Nonlinear dynamics near exceptional points of synthetic antiferromagnetic spin-torque oscillators

R. A. Duine,[1,2] V. Errani,[1,*,†] and J. S. Harms[1,*,‡]
[1]*Institute for Theoretical Physics, Utrecht University, 3584CC Utrecht, The Netherlands*
[2]*Department of Applied Physics, Eindhoven University of Technology, P.O. Box 513, 5600 MB Eindhoven, The Netherlands*

(Received 1 March 2023; accepted 20 July 2023; published 21 August 2023)

We consider a synthetic antiferromagnetic spin-torque oscillator (STO) with anisotropic interlayer exchange coupling. This system exhibits exceptional points (EPs) in its linearized dynamics. We find the nonlinear dynamics and the dynamical phase diagram of the system both analytically and numerically. Moreover, we show that, near one of the EPs, the power of the oscillator depends extremely sensitively on the injected spin current. Our findings may be useful for designing sensitive magnetometers and for other applications of STOs.

DOI: 10.1103/PhysRevB.108.054428

I. INTRODUCTION

For the design of many applications, such as magnetometers, converters, and amplifiers, a strong response to perturbations is preferred. One way to achieve this strong response is to make use of the existence of exceptional points (EPs) [1–3]. EPs are characterized by a square-root dependence of the imaginary part of the eigenfrequencies on some system parameters, which enables a large dynamic response as a result of a small change in a parameter. Mathematically, EPs correspond to the coalescence of different eigenvalues and eigenvectors in parameter space [4,5]. EPs are studied intensely since they might lead to better sensors [1–3], yield a variety of interesting phenomena such as lasing [6] and spontaneous emission [7], and give rise to geometric phases when encircling them [8]. Examples of physical systems that exhibit EPs are optical microcavities [9] and other photonic systems [3,10], optical lattices with engineered defects [11], electromechanical systems [12], superconducting resonators [13], nodal superconductors [9], semimetals [14–16], and magnetic systems [17–23]. While EPs have been studied intensely in the linear regime, the nonlinear regime remains relatively unexplored.

In this paper, we consider a synthetic antiferromagnetic (SAFM) spin-torque oscillator (STO), i.e., a STO that consists of two magnetic layers that are coupled by Ruderman-Kittel-Kasuya-Yosida (RKKY) interactions. We consider the situation that one of the two magnetic layers is driven by means of the injection of spin current. This could be achieved by spin-orbit torque or by spin-transfer torque [24]. Generically, an STO is a magnetic system in which the damping is compensated by the injection of spin angular momentum from a spin current to yield precessional magnetic dynamics [23,25–27]. These oscillators have potential for a wide range of applications, such as detectors, microwave signal sources [28,29], microwave-assisted magnetic recording, and neuromorphic computation [30,31].

The SAFM STO that we consider has anisotropic RKKY coupling and exhibits EPs in its linearized dynamics. We consider the full nonlinear dynamics analytically and find the limit cycles of the magnetization dynamics. Moreover, we show that the dynamics becomes relatively simple close to the EPs because the power and precessing frequency depend linearly on the injected spin current. These analytical results agree with numerical computations and lead to a complete understanding of the steady-state behavior of the system. Furthermore, we find from our analysis that the magnetization dynamics is extremely sensitive to small changes in parameters in the sense that the slope of the steady-state power with respect to injected spin current diverges close to one of the EPs. This result cannot be obtained from a linear analysis, and the nonlinear description is therefore needed. A complementary work to ours is that of Deng *et al.* [23], who numerically consider the nonlinear dynamics of an STO near a different type of EP. Another recent closely related complementary work is that of Ref. [32].

The remainder of this paper is organized as follows. In the next section, we present the model and determine the eigenfrequencies and stability conditions from a linear analysis. In the second section, we consider the nonlinear dynamics close to the EPs and find the limit circles of the magnetic dynamics. In the third section, we consider the magnetization dynamics numerically and find the dynamical phase diagram. We end with a brief conclusion and outlook.

II. LINEAR ANALYSIS

We consider a STO composed of two RKKY-coupled nanomagnets subject to the same external magnetic field and uniaxial anisotropy, see Fig. 1. For simplicity, we take both magnetic layers to be identical. Furthermore, spin angular momentum is injected into the bottom magnetic layer. The magnetic energy is given by

$$E = -B(m_{U,z} + m_{L,z}) - \frac{K\left(m_{U,z}^2 + m_{L,z}^2\right)}{2} - J_\perp(m_{U,x}m_{L,x} + m_{U,y}m_{L,y}) - J_z m_{U,z}m_{L,z}, \quad (1)$$

*These authors contributed equally to this work.
†v.errani@uu.nl
‡j.harms@uu.nl

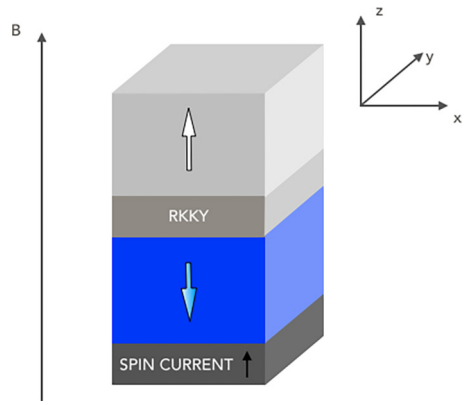

FIG. 1. A synthetic antiferromagnetic spin-torque oscillator in an external magnetic field $B\hat{z}$. Spin angular momentum is injected into the bottom magnetic layer.

where U denotes the upper and L the lower macrospin, and $m_{L/U,i}$ the ith Cartesian component of the macrospin. Furthermore, K is the uniaxial anisotropy constant, $B > 0$ the external magnetic field directed along the z axis, $J_\perp$ the in-plane RKKY interaction, and J_z its out-of-plane component. We take the RKKY interaction to be anisotropic because, first of all, it will typically be anisotropic, and second, the anisotropic coupling enriches the phase diagram.

For temperatures below the Curie temperature, the magnetization dynamics is well described by the Landau-Lifschitz-Gilbert (LLG) equation with the inclusion of the injected spin current:

$$\frac{\partial \mathbf{m}_\nu}{\partial t} = -\mathbf{m}_\nu \times \mathbf{h}_{\mathrm{eff},\nu} + \alpha \mathbf{m}_\nu \times \frac{\partial \mathbf{m}_\nu}{\partial t} + I_{s,\nu} \mathbf{m}_\nu \times (\mathbf{m}_\nu \times \hat{z}), \tag{2}$$

with the effective field $\mathbf{h}_{\mathrm{eff},\nu} = -\gamma \delta E/\delta \mathbf{m}_\nu$. Here, ν denotes either the lower (L) or the upper (U) macrospin, α the dimensionless Gilbert damping, and $I_{s,U} = 0$, $I_{s,L} = I_s > 0$ the spin current. The sign of the spin current is such that it tends to align the bottom magnetic layer against the external field. Since the Gilbert damping is typically small $\alpha \ll 1$, we work in most of what follows to lowest order in α and discard terms of the order αI_s as well. Furthermore, we set $\gamma = 1$ so that B, K, $J_\perp$, and J_z have units of frequency.

For the case that $K > 0$, the magnetic energy in Eq. (1) yields four configurations where the torques on the magnetization direction in both layers vanish simultaneously: These are both layers pointing up, both pointing down, and the two antiparallel configurations. Depending on the parameters, these configurations are energy extrema that are stable or unstable. For large fields, the configuration with both spins pointing up is stable. For large spin currents, the bottom layer is forced to point downward, while depending on the strength and sign of the RKKY coupling, the top layer may point down or up.

The most interesting configuration for our purposes is the antiparallel configuration. As we shall see below, the linearized dynamics around this configuration yields an EP. This may be anticipated because, in the absence of dissipation, i.e., when $\alpha = 0$ and $I_s = 0$, the antiparallel configuration in an external field is reminiscent of a system of two coupled harmonic oscillators with one of the oscillators having a potential energy that is inverted. This latter system is known to yield an EP [33]. Because $I_s > 0$, we consider the situation where the bottom magnetic layer is pointing against the field.

We investigate the stability of a given magnetic state by linearizing the LLG equations for small deviations around that state. For the reasons mentioned above, we focus on the antiparallel configuration with the magnetization of the bottom layer pointing against the external field, which yields the eigenfrequencies:

$$\begin{aligned}(\alpha^2+1)\omega_\pm &= B - \mathrm{i}\alpha(K - J_z) - \frac{(\mathrm{i}-\alpha)I_s}{2} \\ &\pm \sqrt{\left[K - J_z - \mathrm{i}\alpha B + \frac{(\mathrm{i}-\alpha)I_s}{2}\right]^2 - (\alpha^2+1)J_\perp^2}. \end{aligned} \tag{3}$$

From this expression, we find the parameters for which the system exhibits an EP by setting the expression under the square root equal to zero. To lowest order in α and I_s, this yields $J_\perp^2 = (K - J_z)^2$ and $I_s = 2\alpha B$. Close to this EP and particularly when the expression underneath the square root is negative, the imaginary part of the eigenvalues depends strongly on small changes in parameters. Physically, this implies that a small change in parameters may yield a strong dynamic response because a positive imaginary part of the eigenfrequency corresponds to exponential growth of small-amplitude fluctuations. By determining when the imaginary part of the above eigenfrequency changes sign, we find that the antiparallel configuration is stable when

$$\frac{I_s}{2\alpha} > \frac{-K - J_z + |K - J_z|B/\sqrt{(K-J_z)^2 - J_\perp^2}}{1 + |K - J_z|/\sqrt{(K-J_z)^2 - J_\perp^2}}, \tag{4a}$$

$$\frac{I_s}{2\alpha} < \frac{-K - J_z - |K - J_z|B/\sqrt{(K-J_z)^2 - J_\perp^2}}{1 - |K - J_z|/\sqrt{(K-J_z)^2 - J_\perp^2}}. \tag{4b}$$

In the next section, we focus on the nonlinear dynamics outside this range of dynamical stability. As we shall see, the power of the STO is extremely sensitive to small changes in the current around this EP for $K > 0$ but not when $K < 0$.

III. NONLINEAR DYNAMICS

In this section, we discuss the nonlinear dynamics of the system described in Sec. II and specifically focus on the limit cycles of the model.

The reactive dynamics is formulated by means of the Poisson bracket $\{m_\alpha, m_\beta\} = \epsilon_{\alpha\beta\gamma} m_\gamma$. From here, we define the canonical coordinates $p_{U/L} = m_{U/L,z}$ and $\theta_{U/L} = \arctan(m_{U/L,y}/m_{U/L,x})$ that correspond to the total power and angle of the oscillator and which have nonzero Poisson brackets $\{p_{U/L}, \theta_{U/L}\} = 1$. We continue performing yet another coordinate transformation that makes use of the rotational symmetry around the z axis:

$$\begin{aligned} \mu &= \frac{p_U + p_L}{2}, \quad & \eta &= \frac{p_U - p_L}{2}, \\ \theta &= \theta_U + \theta_L, \quad & \phi &= \theta_U - \theta_L, \end{aligned} \tag{5}$$

where $\mu \in [-1, 1]$ and $\eta \in [-1+\mu, 1-\mu]$. The above coordinates have $\{\mu, \theta\} = 1$ and $\{\eta, \phi\} = 1$ as nonvanishing Poisson brackets. In these coordinates, the Hamiltonian (internal energy) in Eq. (1) becomes

$$h \equiv E = -2B\mu - K(\mu^2+\eta^2) - J_z(\mu^2-\eta^2) - J_\perp\sqrt{[1-(\mu+\eta)^2][1-(\mu-\eta)^2]}\cos(\phi), \quad (6)$$

where the rotation symmetry around the z axis ensures that the right-hand side does not depend on θ. The Hamiltonian equations of motion are accordingly given by

$$\dot{\mu} = \{\mu, E\} = \{\mu, \theta\}\partial_\theta E = 0, \quad (7a)$$

$$\dot{\theta} = 2B + 2(K+J_z)\mu - \frac{2J_\perp\mu(1+\eta^2-\mu^2)\cos(\phi)}{\sqrt{[1-(\mu+\eta)^2][1-(\mu-\eta)^2]}}, \quad (7b)$$

$$\dot{\phi} = 2(K-J_z)\eta - \frac{2J_\perp\eta(1+\mu^2-\eta^2)\cos(\phi)}{\sqrt{[1-(\mu+\eta)^2][1-(\mu-\eta)^2]}}, \quad (7c)$$

$$\dot{\eta} = 2J_\perp\sqrt{[1-(\mu+\eta)^2][1-(\mu-\eta)^2]}\sin(\phi), \quad (7d)$$

where the rotation symmetry guarantees that the total power is conserved. For the limit cycles, we expect $\dot{\phi} = \dot{\eta} = 0$ since both spins experience the same magnetic field strength and are thus expected to have equal angular velocity. Using this ansatz, we find two possible expressions for the difference in power η in terms of the total power μ for $J_\perp^2 < K^2$, which are given by

$$\eta = 0, \quad \eta^2 = 1+\mu^2 - \frac{2|K-J_z||\mu|}{\sqrt{(K-J_z)^2 - J_\perp^2}}. \quad (8)$$

In case $J_\perp^2 > (K-J_z)^2$, we are only left with $\eta = 0$ as a solution since we require η to be real.

The model under consideration furthermore has dissipative contributions in the form of Gilbert damping and the injection of spin angular momentum. Up to first order in the Gilbert damping, constant α, the dynamics of total power μ, and the relative power η due to Gilbert damping is given by

$$\frac{\dot{\mu}}{\alpha} = [B+(K+J_z)\mu](1-\mu^2-\eta^2) - 2(K-J_z)\eta^2\mu - J_\perp\sqrt{[1-(\mu+\eta)^2][1-(\mu-\eta)^2]}\cos(\phi)\mu, \quad (9a)$$

$$= B(1+\mu^2-\eta^2) + [h+J_z+K(1-2\eta^2)]\mu, \quad (9b)$$

$$\frac{\dot{\eta}}{\alpha} = \{-2B\mu + K(1-3\mu^2-\eta^2) - J_z(1+\mu^2-\eta^2) - J_\perp\sqrt{[1-(\mu+\eta)^2][1-(\mu-\eta)^2]}\cos(\phi)\}\eta, \quad (9c)$$

$$= [h+K(1-2\mu^2)-J_z]\eta. \quad (9d)$$

The influence of SOT, up to first order in I_s, on the dissipative dynamics is, on the other hand, given by

$$\frac{\dot{\mu}}{I_s} = \frac{(\mu-\eta)^2-1}{2}, \quad (10a)$$

$$\frac{\dot{\eta}}{I_s} = \frac{1-(\mu-\eta)^2}{2}. \quad (10b)$$

With this set up, we are in the position to discuss the limit cycles of the model and their stability. Again, for all values of $J_\perp$, $\eta = 0$ will be a solution of $\dot{\phi} = \dot{\eta} = 0$. Furthermore, for $J_\perp^2 < K^2$, we additionally have $\eta^2 = 1+\mu^2-2|K||\mu|/\sqrt{K^2-J_\perp^2}$ as a solution. Below, we address limit cycles and stability for the solution $\eta = 0$, which covers, as we shall see, the behavior near the EP. For completeness, we address the other type of limit cycles and their stability in Appendixes A–D.

When $\eta = 0$, the equation for the total power μ becomes

$$\frac{\dot{\mu}}{\alpha} = \left[B - \frac{I_s}{2\alpha} + (K+J_z-|J_\perp|)\mu\right](1-\mu^2). \quad (11)$$

This has two solutions:

$$\mu = \pm 1, \quad \mu = \frac{B-\frac{I_s}{2\alpha}}{|J_\perp|-J_z-K}, \quad (12)$$

with $\mu = m_{U,z} = m_{L,z}$. The first solution describes both macrospins aligning in the $\pm\hat{z}$ direction. The second solution, on the other hand, describes the limit cycle toward which the system converges for sufficiently large times. Furthermore, this limit cycle has a precessional frequency of

$$\dot{\theta} = \frac{I_s}{\alpha}. \quad (13)$$

From the fixed point analyses presented in Appendix B, these fixed points are stable if $\partial_\mu\dot{\mu} < 0$ and $|J_\perp|(1+\mu^2) > (K-J_z)(1-\mu^2)$. Alternatively, these limit cycles are unstable if one of the above constraints is not satisfied. The limit cycle solution $\mu = (B-I_s/2\alpha)/(|J_\perp|-J_z-K)$ is thus stable if $\max[K+J_z, (K-J_z)(1-\mu^2)/(1+\mu^2)] < |J_\perp|$. While the static solution with $\mu = \pm 1$, on the other hand, is stable if $\mp(B-I_s/2\alpha) < K+J_z-|J_\perp|$.

In conclusion, we find that the power of the SAFM is quite sensitive to small perturbations around the point $|J_\perp| \gtrsim K+J_z$, where the slope of the total power $\mu = m_{U,z} = m_{L,z}$ with respect to $I_s/2\alpha$ is given by $(|J_\perp|-J_z-K)^{-1}$ in Eq. (12). The total power of the oscillator therefore depends sensitively on injected spin current around this point. Hence, we find an enhanced sensitivity if $K+J_z > 0$ for $J_\perp > K+J_z$.

IV. NUMERICAL RESULTS

In this section, we determine all the dynamical phases of the SAFM oscillator using numerical solutions. For concreteness, we focus on the case that $J_z = 0$. We solve the LLG Eq. (2) numerically for different values of the coupling $J_\perp$ and current I_s starting from the antiparallel configuration with a small initial perturbation. In Fig. 2, we present the long-time behavior in each region of the dynamical phase diagram, with the blue spin denoting the magnetic layer that is driven by spin current. We note that a change in the external magnetic field B results in a rigid upward or downward shift of the phase diagram. The black lines in Fig. 2 are the analytically predicted phase boundaries from Eqs. (4) and (12). We find very good agreement between the analytic predictions and the results from numerical solutions.

There are three regions where the spin configuration is static (I, II, and III), and one region, IV, where the magnetization is oscillating. The region in Fig. 2 with $J_\perp < K$ may be interpreted in the following way. If we start from zero coupling and increase the current, we observe that the configuration is initially parallel with both macrospins aligned upward

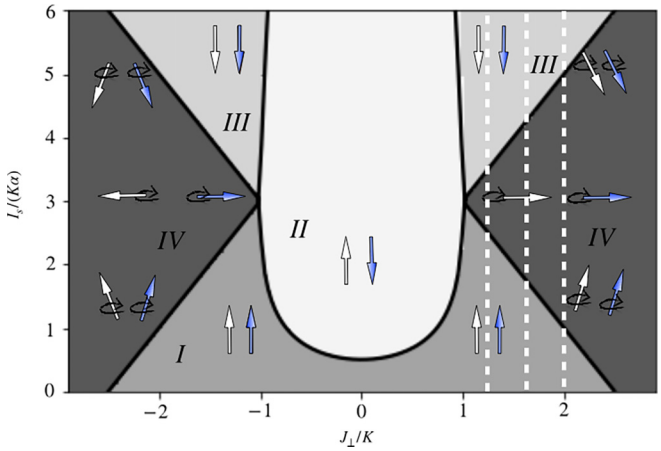

FIG. 2. Dynamical phase diagram for $K > 0$ as a function of coupling $J_\perp$ and current I_s. The analytical predictions from Eqs. (4) and (12) are plotted as the black lines. The steady-state configuration is indicated for each region. Region IV corresponds to oscillations. The z component of the magnetization in this region depends on the injected spin current. We took $B/K = 1.5$ and $J_z = 0$.

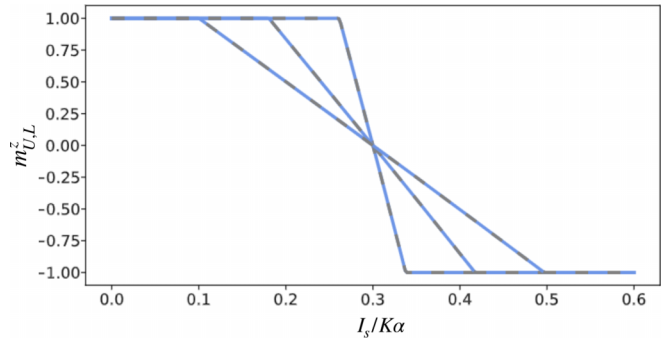

FIG. 3. Plot of the z direction of the macrospins in both synthetic layers as a function of the current I_s. The three different lines correspond to different values in the coupling strength ($J_\perp/K = 1.2, 1.6, 2$), with the steeper slope corresponding to decreasing $J_\perp$. These values are depicted by the dotted lines in Fig. 2. Parameters taken are $B/K = 1.5$ and $J_z = 0$.

(region I). This is what we expect since, for small values of the current, the spin current is not large enough to compensate the Gilbert damping, and the two macrospins both align with the external magnetic field. Increasing the current further, the system can keep the initial configuration (region II) since now the current is enough to compensate for the damping (light-blue macrospin pointing downward), but the coupling is too small to make the white macrospin, i.e., the magnetic layer into which no spin current is injected, flip. Indeed for increasing values of the coupling and sufficiently high current, both macrospins are aligned against the external field (region III).

When considering the nonlinear behavior beyond the EP, region IV is of most interest. In this region, the two macrospins are oscillating, with a frequency I_s/α depending only on the current I_s and the damping α. These two macrospins exhibit nearly parallel orientations for positive values of the coupling and antiparallel orientations for negative values. In Fig. 3, we show the z component of the magnetization as a function of the current I_s, in which the different lines correspond to the vertical dashed lines in Fig. 2. The numerical simulations confirm that the current and the macrospin orientation are related in a linear way given by Eq. (12).

We have focused on the situation that $J_z = 0$, which is the most interesting because all four phases (I–IV) meet at one point. In fact, starting from Fig. 2 and increasing J_z, only the three regions I, III, and IV meet at the two points since the antiparallel region progressively shrinks and the points shift outward. If instead we consider negative values of J_z, the antiparallel region progressively enlarges, and region I decreases.

V. DISCUSSION AND CONCLUSIONS

We analytically and numerically explored the nonlinear behavior of a synthetic antiferromagnetic STO with anisotropic RKKY coupling. We found that the EP which is found in its linearized dynamics leads to enhanced sensitivity of the power of the oscillator, particularly as a function of injected spin current. This enhanced sensitivity may be used to engineer magnetometers or sensors of spin current. Furthermore, recent work shows that it is possible to use spin-torque nano-oscillators to implement different computing schemes and to classify waveforms [31]. Moreover, STOs may be used as tunable spin-wave emitters that excite a specific spin wave depending on the current. We expect that the enhanced sensitivity we predict is an asset for such applications.

Regarding the experimental realization of our model, an ingredient is the anisotropic interlayer coupling. This anisotropic exchange coupling is not essential but makes the phase diagram much richer. Anisotropic exchange coupling has been proposed and experimentally observed in Refs. [34,35]. The required anisotropies may be engineered by interfaces with heavy metals and/or engineering the shape of the magnetic layers, whereas the interlayer coupling may be tuned by varying the thickness of the nonmagnetic spacer. In our approach, we have relied on a macrospin approximation. This is a good description and is in agreement with micromagnetic simulation and experimental results for STOs with diameters <30 nm [36].

Future work could focus on the inclusion of thermal fluctuations. We expect that these will affect the phase but not the orientation or the amplitude of the oscillations. Finally, we hope that our work, together with that of Deng *et al.* [23], inspires the operation of STOs near EPs. In fact, while resubmitting this paper, a recent preprint appeared [37] in which authors have experimentally observed EPs in STOs, albeit in a setup that is slightly different from ours.

ACKNOWLEDGMENTS

J.S.H. would like to thank W. Q. Boon for fruitful discussions. R.A.D. acknowledges support as a member of the D-ITP consortium, a program of the Netherlands Organisation for Scientific Research (NWO) that is funded by the Dutch Ministry of Education, Culture and Science (OCW). R.A.D. acknowledges the funding from the European Research Council (ERC) under the European Union's Horizon 2020 research and innovation programme (Grant No. 725509). This paper

is part of the Fluid Spintronics research programme with Project No. 182.069, which is financed by the Dutch Research Council (NWO).

R.A.D. conceived the project, V.E. and J.S.H. performed the linear analysis, V.E. wrote the numerical codes and numerically constructed the phase diagram, and J.S.H. performed the analytic nonlinear analysis. V.E. and J.S.H. wrote the first draft after which all coauthors contributed to finalizing it.

APPENDIX A: SECOND TYPE OF LIMIT CYCLES FOR $J_\perp^2 < K^2$ FOR $J_z \to 0$

For $J_\perp^2 < K^2$, we also need to consider $\eta^2 = 1 + \mu^2 - 2|K||\mu|/\sqrt{K^2 - J_\perp^2}$ as a solution to $\dot\phi = \dot\eta = 0$. Using the above ansatz, we find that Eqs. (9a) and (10a) give

$$\begin{aligned}\frac{\dot\mu}{\alpha} = &\left[B + K\mu - \frac{I_s}{2\alpha}\right]\left[-2\mu^2 + \frac{2|K||\mu|}{\sqrt{K^2 - J_\perp^2}}\right] \\ &- \mu\frac{J_\perp^2}{K}\frac{2|K||\mu|}{\sqrt{K^2 - J_\perp^2}} - 2K\mu\left[1 + \mu^2 - \frac{2|K||\mu|}{\sqrt{K^2 - J_\perp^2}}\right] \\ &- \frac{I_s}{\alpha}\mathrm{sgn}(\eta)\mu\sqrt{1 + \mu^2 - \frac{2|K||\mu|}{\sqrt{K^2 - J_\perp^2}}}. \end{aligned} \tag{A1}$$

In the first instance, we note that $\mu = 0$ gives a static solution to the above equation. This describes the configuration in Fig. 1, in which two spins point in opposite directions. From Appendix C, it follows that a requirement for stability of this phase is $\partial_\mu\dot\mu < 0$ at the fixed point. This requirement for stability, with $\mathrm{sgn}(\eta) = 1$, becomes

$$\frac{I_s}{2\alpha} > \frac{-K + \frac{|K|B}{\sqrt{K^2 - J_\perp^2}}}{1 + \frac{|K|}{\sqrt{K^2 - J_\perp^2}}}, \tag{A2a}$$

$$\frac{I_s}{2\alpha} < \frac{-K - \frac{|K|B}{\sqrt{K^2 - J_\perp^2}}}{1 - \frac{|K|}{\sqrt{K^2 - J_\perp^2}}}. \tag{A2b}$$

These are precisely the same conditions as in Eq. (4) for $J_z \to 0$. The fixed point with $\mathrm{sgn}(\eta) = -1$, on the other hand, is stable if

$$\frac{I_s}{2\alpha} > \frac{-K + \frac{|K|B}{\sqrt{K^2 - J_\perp^2}}}{-1 + \frac{|K|}{\sqrt{K^2 - J_\perp^2}}}, \tag{A3a}$$

$$\frac{I_s}{2\alpha} < \frac{K + \frac{|K|B}{\sqrt{K^2 - J_\perp^2}}}{1 + \frac{|K|}{\sqrt{K^2 - J_\perp^2}}}. \tag{A3b}$$

We see that the configuration with $\mathrm{sgn}(\eta) = -1$ is always unstable since there is no interval for stability.

To make progress in the regime where we expect limit cycles, we rewrite Eq. (A1):

$$\begin{aligned} g(I_s, \mu) &= \frac{\dot\mu}{\alpha|\mu|} \\ &= (1 - 2\epsilon|\mu|)\left[2K[\mu - \mathrm{sgn}(\mu)\epsilon] + \left(B - \frac{I_s}{2\alpha}\right)\right] \\ &\quad - \mathrm{sgn}(\mu)\epsilon\frac{I_s}{\alpha}\eta(\mu), \end{aligned} \tag{A4}$$

where $\epsilon \equiv \sqrt{K^2 - J_\perp^2}/2|K| \in (0, \frac{1}{2})$. Let us analyze the above equation in a bit more detail. We assume that $\mu > 0$ at the fixed point. From here, we find that Eq. (A4) implies

$$\frac{I_s}{2\alpha} = \frac{B + 2K(\mu - \epsilon)}{1 + \frac{2\epsilon\eta}{1 - 2\epsilon\mu}}. \tag{A5}$$

From Appendix C, we find the stability requirement $\dot\mu \leqslant 0$ for limit cycles of Eq. (A4) to be

$$\frac{I_s}{2\alpha}\frac{1 - 4\epsilon^2}{(1 - 2\epsilon\mu)^2} + 2K\eta < 0. \tag{A6}$$

We would like to find the minimal current I_s for these limit cycles to be stable; hence, we would like to find the current for which Eq. (A6) is zero, in other words, $\partial_\mu\dot\mu = \partial_\mu g(I_s, \mu)|_{I_s(\mu)} = 0$. On the other hand, we know $g[I_s(\mu), \mu] = 0$ is the limit cycle—fixed point—condition. From here, we find $d_\mu g[I_s(\mu), \mu] = (\partial_{I_s} g)(\partial_\mu I_s) + \partial_\mu g = 0$, and hence, $\partial_\mu I_s = 0 \leftrightarrow \partial_\mu g \equiv \partial_\mu\dot\mu = 0$. Thus, when looking for the critical current, it is sufficient to consider $\partial_\mu I_s = 0$. We proceed by writing Eq. (A5) as

$$\frac{(1 - 2\epsilon\mu + 2\epsilon\eta)I_s}{2\alpha} = (1 - 2\epsilon\mu)[B + 2K(\mu - \epsilon)].$$

Furthermore, we take the derivative with respect to μ of the above and note that we are considering points which satisfy $\partial_\mu I_s = 0$. This leaves us with

$$\begin{aligned}&\frac{(1 - 2\epsilon\mu + 2\epsilon\eta)I_s}{2\alpha} \\ &\quad = \{2\epsilon[B + 2K(\mu - \epsilon)] + 2K(1 - 2\epsilon\mu)\}\eta.\end{aligned}$$

which according to Eq. (A5) gives us

$$\begin{aligned}&(1 - 2\epsilon\mu)[B + 2K(\mu - \epsilon)] \\ &\quad = [2\epsilon B - 2K(1 - 4\epsilon\mu + 2\epsilon^2)]\eta.\end{aligned} \tag{A7}$$

To proceed, we assume $\eta^2 \ll 1$ around the critical current. A consequence of the above is that we assume $\mu_\epsilon - \delta\mu \ll 1$ with

$$\mu_\epsilon = \frac{1}{2\epsilon}(1 - \sqrt{1 - 4\epsilon^2}), \tag{A8}$$

and from relation in Eq. (8), we see that $\eta^2 \sim (2\epsilon)^{-1}\sqrt{1 - 4\epsilon^2}\,\delta\mu$ at linear order in $\delta\mu$ and η^2. By squaring Eq. (A7) and expanding up to linear order in $\delta\mu$, we find the solution to be

$$2\delta\mu \sim \sqrt{\frac{1}{4\epsilon^2} - 1}\frac{[K(1 - 2\epsilon^2 - \sqrt{1 - 4\epsilon^2}) + \epsilon B]^2}{[K(1 - 2\epsilon^2 - 2\sqrt{1 - 4\epsilon^2}) + \epsilon B]^2}. \tag{A9}$$

Accordingly, the critical current is well approximated by using Eq. (A5):

$$I_{s,c} \simeq I_s(\mu_\epsilon - \delta\mu). \tag{A10}$$

We thus have two forms of stable limit cycles for $-|J_\perp| < K < 0$ and $I_s > I_{s,c}$, namely, one described in Sec. III, where $\eta = 0$, and one with $\eta \neq 0$, which we described in this Appendix.

APPENDIX B: STABILITY REQUIREMENTS FOR LIMIT CYCLES WITH $\eta = 0$

To perform the stability analyses, we first determine the fixed points in ϕ and η up to first order in dissipative terms. Including dissipative corrections, Eq. (7) becomes

$$\delta\dot{\eta} = 4|J_\perp|(1-\mu^2)\delta\phi_{\rm fp} - \frac{I_s}{2}(1-\mu^2) = 0. \tag{B1}$$

The above implies $\delta\phi_{\rm fp} = I_s/8|J_\perp|$. We continue the stability analyses by linearizing around the fixed point $\eta = 0$, $\sin(\phi) = I_s/4J_\perp$, and $\mu = (B - I_s/2\alpha)/(|J_\perp| - K)$:

$$\begin{pmatrix}\dot{\phi}\\ \dot{\eta}\\ \dot{\mu}\end{pmatrix} = \begin{pmatrix}0 & \gamma_\eta^\phi & 0\\ \gamma_\phi^\eta & \epsilon_\eta^\eta & 0\\ 0 & \epsilon_\eta^\mu & \epsilon_\mu^\mu\end{pmatrix}\begin{pmatrix}\delta\phi\\ \delta\eta\\ \delta\mu\end{pmatrix}, \tag{B2}$$

where γ is zeroth order in α and I_s, and ϵ is first order in dissipation. The eigenvalues λ of the above matrix are given by

$$\left(\epsilon_\mu^\mu - \lambda\right)\left[\left(\epsilon_\eta^\eta - \lambda\right)\lambda - \gamma_\phi^\eta\gamma_\eta^\phi\right] = 0. \tag{B3}$$

Hence, one eigenvalue is given by ϵ_μ^μ, and the real part of the other two eigenvalues is given by ϵ_η^η. The fixed point is stable if the real part of all eigenvalues is negative. The constraint $\epsilon_\mu^\mu < 0$ precisely gives $\partial_\mu\dot{\mu} < 0$ in Eq. (11). The requirement that $\epsilon_\eta^\eta < 0$, on the other hand, gives $\epsilon_\eta^\eta/\alpha = (K - J_z)(1-\mu^2) - |J_\perp|(1+\mu^2) < 0$, which is satisfied for $K - J_z < |J_\perp|$.

APPENDIX C: STABILITY REQUIREMENTS FOR LIMIT CYCLES WITH $\eta \neq 0$

In the case $\eta \neq 0$, the angle ϕ shifts due to dissipative corrections on Eq. (7). We denote this shift by $\delta\phi_{\rm fp}$. We find that the linearized equations of motion around the fixed point give

$$\begin{pmatrix}\dot{\phi}\\ \dot{\eta}\\ \dot{\mu}\end{pmatrix} = \begin{pmatrix}\epsilon_\phi^\phi & \gamma_\eta^\phi & \gamma_\mu^\phi\\ \gamma_\phi^\eta & \epsilon_\eta^\eta & \epsilon_\mu^\eta\\ 0 & \epsilon_\eta^\mu & \epsilon_\mu^\mu\end{pmatrix}\begin{pmatrix}\delta\phi\\ \delta\eta\\ \delta\mu\end{pmatrix}, \tag{C1}$$

with γ zeroth order in α and I_s, and ϵ first order in dissipation. The eigenvalues λ of the above matrix are given by the third-order polynomial equation:

$$\begin{aligned}&\left(\epsilon_\mu^\mu - \lambda\right)\left[\left(\epsilon_\phi^\phi - \lambda\right)\left(\epsilon_\eta^\eta - \lambda\right) - \gamma_\mu^\eta\gamma_\eta^\phi\right]\\ &\quad + \gamma_\mu^\eta\gamma_\mu^\phi\epsilon_\eta^\mu - \epsilon_\mu^\mu\epsilon_\mu^\eta\left(\epsilon_\phi^\phi - \lambda\right) = 0.\end{aligned} \tag{C2}$$

Hence, the eigenvalues—up to first order in α and I_s—are given by $\lambda_1 = \epsilon_\mu^\mu - (\gamma_\mu^\phi/\gamma_\eta^\phi)\epsilon_\eta^\mu$ and $\lambda_\pm = (\epsilon_\phi^\phi + \epsilon_\eta^\eta)/2 \pm \sqrt{\gamma_\phi^\eta\gamma_\eta^\phi} \pm \epsilon_\eta^\mu\gamma_\phi^\eta\gamma_\eta^\phi/\sqrt{\gamma_\phi^\eta\gamma_\eta^\phi}$. Since we are only interested in the real part of the eigenfrequencies for our stability analyses, we find that the limit cycle is stable if

$$\begin{aligned}\mathrm{Re}(\lambda_1) &= \epsilon_\mu^\mu - \left(\frac{\gamma_\mu^\phi}{\gamma_\eta^\phi}\right)\epsilon_\eta^\mu\\ &= \epsilon_\mu^\mu + (\partial_\mu\eta)\epsilon_\eta^\mu = \partial_\mu\dot{\mu} \leqslant 0,\end{aligned} \tag{C3a}$$

$$\mathrm{Re}(\lambda_\pm) = \frac{\epsilon_\phi^\phi + \epsilon_\eta^\eta}{2} \leqslant 0. \tag{C3b}$$

First, we note that $(\epsilon_\phi^\phi + \epsilon_\eta^\eta)/2 = (\mu - \eta)I_s/2\alpha - \mu(B + 2K(\mu - \epsilon)) \leqslant 0$, which implies $\mathrm{sgn}[B + 2K(\mu - \epsilon)]\eta > 0$. This condition is satisfied at the limit cycle. Hence, we are left with the stability condition $\partial_\mu\dot{\mu} \leqslant 0$.

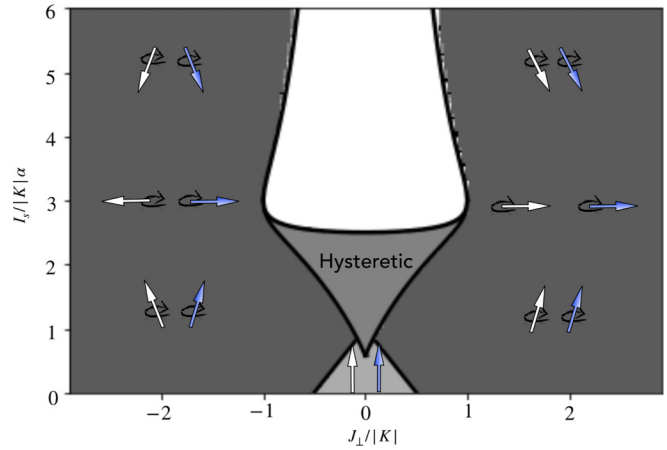

FIG. 4. Numerical phase diagram for the case $K < 0$ as a function of coupling $J_\perp$ and current I_s. In black, the analytical predictions from Eqs. (4), (A2), and (A10) are plotted. In each region, the corresponding long-time configuration is indicated. The regions for large and small $J_\perp$ correspond to oscillations. The z component of the magnetization in this region depends on the injected spin current. The characteristic of the hysteretic region is the dependence of the long-time configuration on the initial conditions. We took $B/K = 1.5$ and $J_z = 0$.

APPENDIX D: PHASE DIAGRAM FOR $K < 0$ WITH $J_z \to 0$

In this Appendix, we describe the phase diagram in the case $K < 0$, which is given in Fig. 4. For $J_\perp^2 > K^2$, this system once again only has limit cycles with $\eta = 0$, and the dynamics of the system is described by Eqs. (12) and (13). On the other hand, when $K^2 < J_\perp^2$, two types of limit cycles are stable if $I_s > I_{s,c}$, as we have seen in Appendixes A and C and Sec. III. One of these limit cycles has $\eta = 0$ and is described by Eqs. (12) and (13). The stability requirement $|J_\perp|(1+\mu^2) > K(1-\mu^2)$ for $K < 0$ in this case leads to $(B - I_s/2\alpha)^2 < (K - J_\perp)^3/(J_\perp + K)$. The second type of limit cycle has $\eta \neq 0$, as discussed in Appendix A, and only exists for current larger then Eq. (A10). We denote the region in Fig. 4 in which both limit cycles exist as the hysteretic regime.

The regions of stable static configurations with $\eta = 1$ and $\mu = 0$ are given by Eqs. (11) and (A2). Additionally, we find the region of stability with $\mu = \pm 1$ and $\eta = 0$ by requiring $\partial_\mu\dot{\mu} < 0$ on Eq. (11). This results in $B - I_s/2\alpha < \mp(K - |J_\perp|)$.

[1] W. Chen, Ş. Kaya Özdemir, G. Zhao, J. Wiersig, and L. Yang, Exceptional points enhance sensing in an optical microcavity, Nature (London) **548**, 192 (2017).

[2] J. Wiersig, Enhancing the Sensitivity of Frequency and Energy Splitting Detection by Using Exceptional Points: Application to Microcavity Sensors for Single-Particle Detection, Phys. Rev. Lett. **112**, 203901 (2014).

[3] M.-A. Miri and A. Alù, Exceptional points in optics and photonics, Science **363**, eaar7709 (2019).

[4] W. Heiss, The physics of exceptional points, J. Phys. A: Math. Theor. **45**, 444016 (2012).

[5] C. Dembowski, H.-D. Gräf, H. L. Harney, A. Heine, W. D. Heiss, H. Rehfeld, and A. Richter, Experimental Observation of the Topological Structure of Exceptional Points, Phys. Rev. Lett. **86**, 787 (2001).

[6] L. Feng, Z. J. Wong, R.-M. Ma, Y. Wang, and X. Zhang, Single-mode laser by parity-time symmetry breaking, Science **346**, 972 (2014).

[7] Z. Lin, A. Pick, M. Lončar, and A. W. Rodriguez, Enhanced Spontaneous Emission at Third-Order Dirac Exceptional Points in Inverse-Designed Photonic Crystals, Phys. Rev. Lett. **117**, 107402 (2016).

[8] C. Dembowski, B. Dietz, H.-D. Gräf, H. L. Harney, A. Heine, W. D. Heiss, and A. Richter, Encircling an exceptional point, Phys. Rev. E **69**, 056216 (2004).

[9] D. Chowdhury, A. Banerjee, and A. Narayan, Exceptional hexagonal warping effect in multi-Weyl semimetals, Phys. Rev. B **105**, 075133 (2022).

[10] Ş. K. Özdemir, S. Rotter, F. Nori, and L. Yang, Parity–time symmetry and exceptional points in photonics, Nat. Mater. **18**, 783 (2019).

[11] S. Longhi and G. Della Valle, Optical lattices with exceptional points in the continuum, Phys. Rev. A **89**, 052132 (2014).

[12] P. Renault, H. Yamaguchi, and I. Mahboob, Virtual Exceptional Points in an Electromechanical System, Phys. Rev. Appl. **11**, 024007 (2019).

[13] M. Partanen, J. Goetz, K. Y. Tan, K. Kohvakka, V. Sevriuk, R. E. Lake, R. Kokkoniemi, J. Ikonen, D. Hazra, A. Mäkinen *et al.*, Exceptional points in tunable superconducting resonators, Phys. Rev. B **100**, 134505 (2019).

[14] J. González and R. A. Molina, Topological protection from exceptional points in Weyl and nodal-line semimetals, Phys. Rev. B **96**, 045437 (2017).

[15] R. A. Molina and J. González, Surface and 3D Quantum Hall Effects from Engineering of Exceptional Points in Nodal-Line Semimetals, Phys. Rev. Lett. **120**, 146601 (2018).

[16] J. M. Lee, T. Kottos, and B. Shapiro, Macroscopic magnetic structures with balanced gain and loss, Phys. Rev. B **91**, 094416 (2015).

[17] H. Yang, C. Wang, T. Yu, Y. Cao, and P. Yan, Antiferromagnetism Emerging in a Ferromagnet with Gain, Phys. Rev. Lett. **121**, 197201 (2018).

[18] T. Yu, H. Yang, L. Song, P. Yan, and Y. Cao, Higher-order exceptional points in ferromagnetic trilayers, Phys. Rev. B **101**, 144414 (2020).

[19] X.-g. Wang, G.-h. Guo, and J. Berakdar, Enhanced Sensitivity at Magnetic High-Order Exceptional Points and Topological Energy Transfer in Magnonic Planar Waveguides, Phys. Rev. Appl. **15**, 034050 (2021).

[20] T. Jeffrey, W. Zhang, and J. Sklenar, Effect of dipolar interaction on exceptional points in synthetic layered magnets, Appl. Phys. Lett. **118**, 202401 (2021).

[21] H. Liu, D. Sun, C. Zhang, M. Groesbeck, R. Mclaughlin, and Z. V. Vardeny, Observation of exceptional points in magnonic parity-time symmetry devices, Sci. Adv. **5**, eaax9144 (2019).

[22] Y. Tserkovnyak, Exceptional points in dissipatively coupled spin dynamics, Phys. Rev. Res. **2**, 013031 (2020).

[23] K. Deng, X. Li, and B. Flebus, Exceptional points as signatures of dynamical magnetic phase transitions, Phys. Rev. B **107**, L100402 (2023).

[24] A. Brataas, A. D. Kent, and H. Ohno, Current-induced torques in magnetic materials, Nat. Mater. **11**, 372 (2012).

[25] J.-V. Kim, Chapter Four—Spin-torque oscillators, Solid State Phys. **63**, 217 (2012).

[26] I. Firastrau, L. Buda-Prejbeanu, B. Dieny, and U. Ebels, Spin-torque nano-oscillator based on a synthetic antiferromagnet free layer and perpendicular to plane polarizer, J. Appl. Phys. **113**, 113908 (2013).

[27] D. Houssameddine, U. Ebels, B. Delaët, B. Rodmacq, I. Firastrau, F. Ponthenier, M. Brunet, C. Thirion, J.-P. Michel, L. Prejbeanu-Buda *et al.*, Spin-torque oscillator using a perpendicular polarizer and a planar free layer, Nat. Mater. **6**, 447 (2007).

[28] V. Tiberkevich, A. Slavin, and J.-V. Kim, Microwave power generated by a spin-torque oscillator in the presence of noise, Appl. Phys. Lett. **91**, 192506 (2007).

[29] J.-R. Chen, A. Smith, E. A. Montoya, J. G. Lu, and I. N. Krivorotov, Spin-orbit torque nano-oscillator with giant magnetoresistance readout, Commun. Phys. **3**, 187 (2020).

[30] T. Chen, R. K. Dumas, A. Eklund, P. K. Muduli, A. Houshang, A. A. Awad, P. Dürrenfeld, B. G. Malm, A. Rusu, and J. Åkerman, Spin-torque and spin-Hall nano-oscillators, Proc. IEEE **104**, 1919 (2016).

[31] D. Marković, N. Leroux, M. Riou, F. Abreu Araujo, J. Torrejon, D. Querlioz, A. Fukushima, S. Yuasa, J. Trastoy, P. Bortolotti *et al.*, Reservoir computing with the frequency, phase, and amplitude of spin-torque nano-oscillators, Appl. Phys. Lett. **114**, 012409 (2019).

[32] S. Komineas, Non-Hermitian dynamics of a two-spin system with PT symmetry, Phys. Rev. B **107**, 094435 (2023).

[33] N. R. Bernier, L. D. Tóth, A. K. Feofanov, and T. J. Kippenberg, Level attraction in a microwave optomechanical circuit, Phys. Rev. A **98**, 023841 (2018).

[34] K. Xia, W. Zhang, M. Lu, and H. Zhai, Noncollinear interlayer exchange coupling caused by interface spin-orbit interaction, Phys. Rev. B **55**, 12561 (1997).

[35] X.-X. Li, J. Bao, L.-Y. Lu, X.-G. Xu, and Y. Jiang, Oscillatory antiferromagnetic interlayer coupling in Co/Pt multilayer with perpendicular anisotropy, Solid State Commun. **148**, 209 (2008).

[36] G. Csaba, M. Pufall, W. Rippard, and W. Porod, Modeling of coupled spin torque oscillators for applications in associative memories, *2012 12th IEEE International Conference on Nanotechnology (IEEE-NANO)* (2012), pp. 1–4.

[37] S. Wittrock, S. Perna, R. Lebrun, K. Ho, R. Dutra, R. Ferreira, P. Bortolotti, C. Serpico, and V. Cros, Non-hermiticity in spintronics: Oscillation death in coupled spintronic nano-oscillators through emerging exceptional points, arXiv:2108.04804.